Quasicontinuum γ decay of ^{91,92}Zr: Benchmarking indirect (n,γ) cross section measurements for the s process

M. Guttormsen,[1,*] S. Goriely,[2] A. C. Larsen,[1] A. Görgen,[1] T. W. Hagen,[1] T. Renstrøm,[1] S. Siem,[1] N. U. H. Syed,[1]
G. Tagliente,[3] H. K. Toft,[1] H. Utsunomiya,[4] A. V. Voinov,[5] and K. Wikan[1]

[1]*Department of Physics, University of Oslo, N-0316 Oslo, Norway*
[2]*Institut d'Astronomie et d'Astrophysique, Université Libre de Bruxelles, Campus de la Plaine, CP-226, 1050 Brussels, Belgium*
[3]*Istituto Nazionale di Fisica Nucleare, 70126 Bari, Italy*
[4]*Department of Physics, Konan University, Okamoto 8-9-1, Higashinada, Kobe 658-8501, Japan*
[5]*Department of Physics and Astronomy, Ohio University, Athens, Ohio 45701, USA*

Nuclear level densities (NLDs) and γ-ray strength functions (γSFs) have been extracted from particle-γ coincidences of the ^{92}Zr$(p,p'\gamma)^{92}$Zr and ^{92}Zr$(p,d\gamma)^{91}$Zr reactions using the Oslo method. The new ^{91,92}Zr γSF data, combined with photonuclear cross sections, cover the whole energy range from $E_\gamma \approx 1.5$ MeV up to the giant dipole resonance at $E_\gamma \approx 17$ MeV. The wide-range γSF data display structures at $E_\gamma \approx 9.5$ MeV, compatible with a superposition of the spin-flip $M1$ resonance and a pygmy $E1$ resonance. Furthermore, the γSF shows a minimum at $E_\gamma \approx 2$–3 MeV and an increase at lower γ-ray energies. The experimentally constrained NLDs and γSFs are shown to reproduce known (n,γ) and Maxwellian-averaged cross sections for ^{91,92}Zr using the TALYS reaction code, thus serving as a benchmark for this indirect method of estimating (n,γ) cross sections for Zr isotopes.

I. INTRODUCTION

The interplay of the microscopic, quantum-mechanical regime and the macroscopic world is crucial for many physical systems. In nuclear astrophysics, various stellar environments and extreme cosmic events represent the playground for the nucleosynthesis, for which nuclear properties determine the outcome together with the astrophysical conditions.

For elements heavier than iron, two neutron-capture processes [1,2] dominate their creation. These two processes are characterized by the time scale, rapid (r) and slow (s), in comparison with the β^--decay rates. Typically, the neutron energies are in the 0.01–1 MeV range, corresponding to stellar temperatures of 0.1–10 GK. The r-process, although the astrophysical site is not yet firmly established [3], takes place at such high neutron densities ($>10^{20}$ cm^{-3}) that the neutron-capture process totally dominates the competing β^- decay until the neutron flux is exhausted. The s-process ($T \sim 0.1$ GK and neutron density $\approx 10^8$ cm^{-3}) operates at much longer time scales, allowing for β^- decay prior to the next neutron capture [1–3].

The weak s-process is believed to take place in massive stars ($M > 8 M_\odot$ [4]) and produces most of the s-abundances in the mass region between Fe and Zr, while the main s-process operates in asymptotic giant branch (AGB) stars and produces the heavier s-process isotopes up to the lead-bismuth region [4].

The neutron-capture cross section is small for isotopes with magic neutron numbers. This results in bottlenecks for the reaction flow, giving rise to the buildup of sharp abundance maxima. This is reflected in the solar-system abundances: We find s-process peaks at mass numbers $A \approx 90, 140$, and 210 corresponding to the magic neutron numbers $N = 50, 82$, and 126, respectively [3].

A crucial question is whether the nuclear system after neutron absorption will keep the neutron and emit γ rays to dissipate the energy, or rather eject the neutron or other particles and/or fragments and thereby produce other elements. For the s-process, this may happen at the so-called *branch points*, where the β^--decay rate is comparable with the (n,γ) rate. The relative probability to keep the neutron depends strongly on the nucleus's ability to emit γ rays, which is governed by the γ-ray strength function (γSF) and the nuclear level density (NLD) of the compound system.

For zirconium isotopes, with semimagic proton number $Z = 40$, and at or close to the $N = 50$ closed shell, neutron-capture cross sections are typically low, and one could question whether statistical approaches such as the Hauser-Feshbach framework [5] are applicable. Further, this is the meeting point of the weak and main s-process, and although ^{96}Zr traditionally has been considered an r-process isotope, it could be significantly produced [6] through neutron capture on the branch-point nucleus ^{95}Zr, depending on its (n,γ) cross section and the neutron flux at the s-process site.

However, since ^{95}Zr is unstable with a half-life of 64 days, no direct (n,γ) cross section measurement has been performed to date, and so only theoretical estimates are available. Recent work has discovered unexpected enhancements in the γSF of several zirconium isotopes, such as the $E1$ pygmy dipole resonance as well as strong $M1$ transitions close to neutron threshold [7,8]. The presence of such enhanced γ-decay probabilities in ^{95}Zr could boost its neutron-capture rate.

Several applications may take advantage of better knowledge of the NLDs and γSFs in the $A \approx 90$ mass region. The production and destruction rates of ^{93}Zr is interesting for the

*magne.guttormsen@fys.uio.no

interpretation of the relative abundance of the radioactive ^{93}Nb and ^{93}Zr pair, which can be used to estimate the *s*-process temperature and also, together with the ^{99}Tc-^{99}Ru pair, act as a chronometer to determine the time elapsed since the start of the *s*-process [9]. The ^{93}Zr(n,γ) cross section has been measured up to 8 keV [10], but contributions to the Maxwellian-averaged cross section at higher energies are based on theoretical calculations and would benefit from experimental constraints [11].

In this work, we report on the NLDs and γ SFs for the ^{91,92}Zr isotopes with neutron number $N = 51$ and 52, respectively, and use our data as input for calculating the ^{90,91}Zr(n,γ) cross sections with the reaction code TALYS [12]. As there exist direct (n,γ) measurements for these isotopes, we use these cases as a benchmark for our indirect method of determining the (n,γ) cross section in this mass region. These investigations are part of a larger campaign to study the branch-point neutron-capture rates at the $A \approx 90$ *s*-process peak.

The outline of the present paper is as follows. In Sec. II, the experiment and results are described. The NLDs and γ SFs are extracted by means of the Oslo method and compared with model calculations in Secs. III and IV, respectively. In Sec. V, radiative neutron-capture cross sections using the TALYS code and experimental NLDs and γ SFs as inputs are compared with known cross sections. A summary and an outlook are given in Sec. VI.

II. EXPERIMENTAL RESULTS

The experiments were performed at the Oslo Cyclotron Laboratory (OCL) with 17-MeV and 28-MeV proton beams for the ^{92}Zr$(p,p')^{92}$Zr and ^{92}Zr$(p,d)^{91}$Zr reactions, respectively. The target was a 2 mg/cm^2 thick metallic foil enriched to 95% in ^{92}Zr.

The charged outgoing particles were measured with the SiRi system of 64 $\Delta E - E$ silicon telescopes with thicknesses of 130 and 1550 μm, respectively [13]. The Si detectors were placed in the forward direction covering $\theta = 42°$ to 54° relative to the beam. The typical energy resolutions measured with the telescopes were 75 and 95 keV full-width half maximum for the $(p,p')^{92}$Zr and $(p,d)^{91}$Zr reactions, respectively. By setting two-dimensional gates on the two $(E, \Delta E)$ matrices, the outgoing charged ejectiles for the desired reactions were selected. Coincident γ rays for the residual ^{91,92}Zr were measured with the CACTUS array [14] consisting of 28 collimated 5 × 5 in. NaI(Tl) detectors with a total efficiency of 14.1% at $E_\gamma = 1.33$ MeV.

The first step in the analysis is to sort the γ-ray spectra as function of excitation energy. Knowing the details of the reaction kinematics, the excitation energy E is given by the energy of the outgoing charged particle. Figure 1 shows the discrete part of the particle-γ matrices (E_γ, E) for the residual ^{91,92}Zr with prompt coincidence requirements. The γ-ray spectra for each excitation energy has been unfolded with new NaI-response functions. The unfolding procedure [15] has proven to work very well also for continuum γ-ray spectra.

The γ-ray multiplicity as function of initial excitation energy E can be calculated by the energy (E) and area (A)
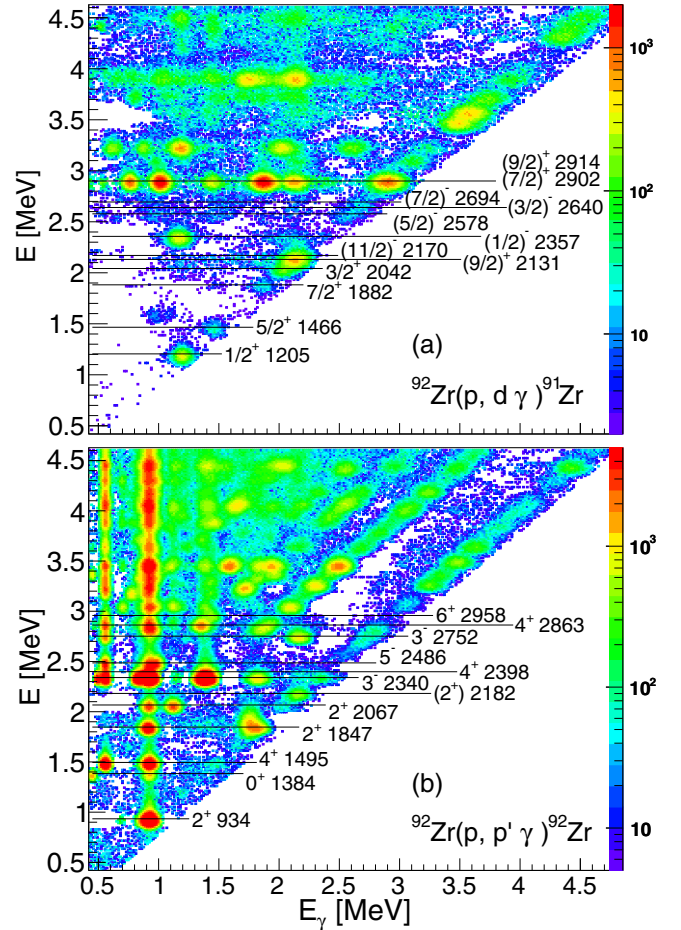

FIG. 1. The discrete part of the particle-γ coincidence matrices for the (a) ^{92}Zr$(p,d)^{91}$Zr and (b) ^{92}Zr$(p,p')^{92}$Zr reactions. Only excitation energies between 0.5 and 4.5 MeV are shown in order to highlight the decay pattern recognized in the present experiment. The pixel width is 16 × 16 keV.

methods [16]:

$$M_\gamma^E(E) = \frac{E}{\langle E_\gamma(E) \rangle}, \qquad (1)$$

$$M_\gamma^A(E) = \frac{A_{\text{total}}(E)}{A_{\text{primary}}(E)}, \qquad (2)$$

where $\langle E_\gamma \rangle$ is the average energy of the total γ-ray spectrum, A_{total} is the intensity (area) of that spectrum, and A_{primary} is the intensity of the primary γ-ray spectrum.

Figure 2 shows the γ-ray multiplicities M_γ^E and M_γ^A for the two reactions. There are practically no statistical errors in the data points due to the high number of counts in the γ-ray spectra. Since M_γ^E represents the most direct and transparent method, we use this quantity as the measure for the multiplicity and M_γ^A as an indicator for systematic errors. We find significant deviation between the two methods only at a few excitation energies. For example, a 60% deviation is found at $E \approx 1.6$ MeV in ^{91}Zr, which is due to a weak contamination peak of $E_\gamma \approx 1$ MeV located where no levels are expected for ^{91}Zr.
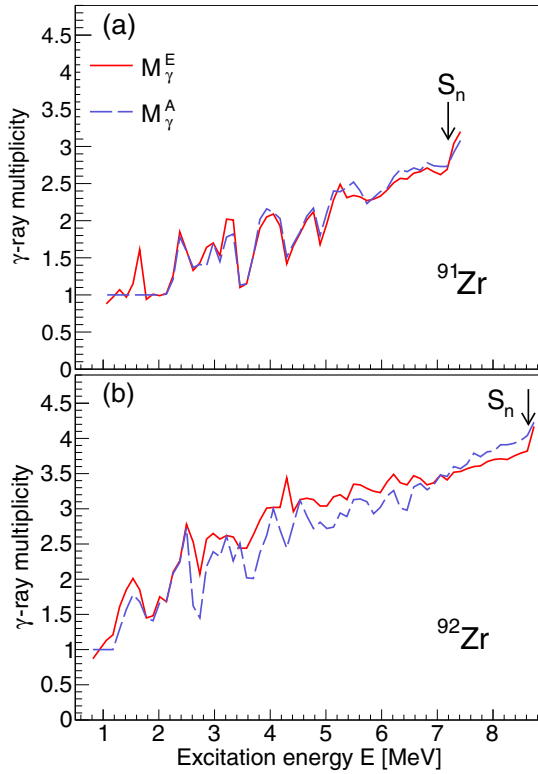
FIG. 2. The γ-ray multiplicity measured as function of excitation energy for the (a) ^{92}Zr$(p,d)^{91}$Zr and (b) ^{92}Zr$(p,p')^{92}$Zr reactions. The energy bin is 120 keV.
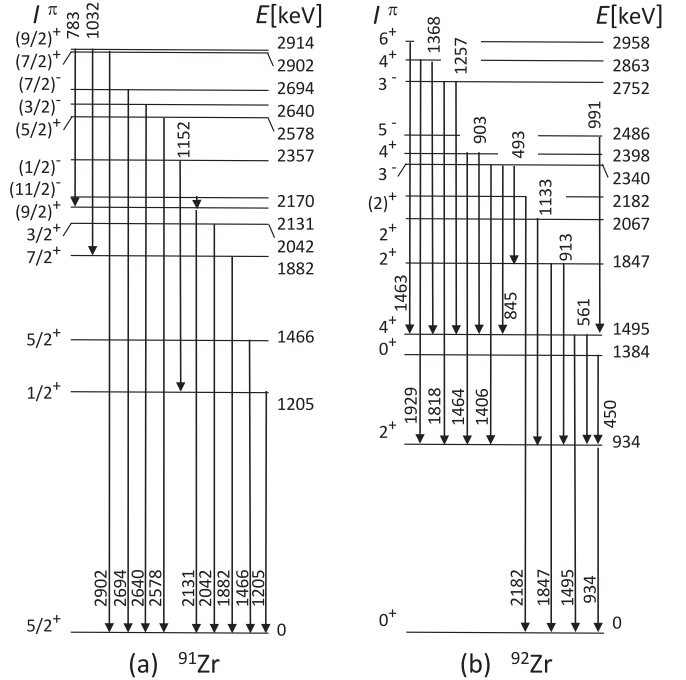

FIG. 3. Partial level schemes for (a) ^{91}Zr and (b) ^{92}Zr. Only the levels which are most strongly populated in the (p,p') and (p,d) reactions, respectively, are shown. The most prominent γ rays from these states are displayed with γ energies in keV. More complete level schemes are found in Ref. [17].

The discrete part of the γ-ray matrices in Fig. 1 are characterized by isolated peaks in the two-dimensional landscape spanned by the initial excitation energy E and the γ-ray energy E_γ. Several peaks tend to fall onto diagonals in the matrices. The diagonal with $E_\gamma \approx E$ represents decay directly to the ground state with a γ-ray multiplicity of $M_\gamma = 1$. We also recognize vertical and horizontal lines in the matrices. The vertical lines correspond to yrast transitions from the last steps in the γ-ray cascades. The horizontal lines appear when levels have high γ-ray multiplicity or several levels are bunched together in excitation energy.

For excitations below $E \approx 3$ MeV, most of the levels and γ transitions seen in the experiment (see Fig. 1) are easily recognized by comparing with known data from literature [17], as displayed Fig. 3. For ^{91}Zr, we see that levels with spin-parity I^π from $1/2^+$ up to $(9/2^+)$ or even $(11/2^-)$ are populated in the (p,d) reaction, as also reported by Blok *et al.* [18]. The population of the latter two high-spin states are due to $\ell = 4$ and (5) transfer, probably involving the $g_{9/2}$ and $h_{11/2}$ neutron orbitals. A peculiar situation is seen for the $(1/2)^-$ 2357-keV level, which shows only one peak at $E_\gamma \approx 1.18$ MeV. The peak is actually the composition of two transitions with almost the same γ energies (1152 and 1205 keV). This is consistent with the γ-ray multiplicity of $M_\gamma \approx 2$ shown in Fig. 2.

Figure 1(b) shows that the inelastic proton reaction on ^{92}Zr populates a broad spin window ranging from 0^+ to 6^+. Since the ground-state spins of ^{91,92}Zr are $5/2^+$ and 0^+, Fig. 2 reveals about one unit more of multiplicity for ^{92}Zr compared to ^{91}Zr.

Only levels of the lowest part of the spin distribution of ^{92}Zr can directly decay to the 0^+ ground state. This is manifested by the dominant feeding into the diagonals of the first excited 2^+ and 4^+ states in Fig. 1. We also observe the vertical lines corresponding to the transitions $4^+ \rightarrow 2^+$ (561 keV) and $2^+ \rightarrow 0^+$ (934 keV). As an example, the multiplicity spectrum of ^{92}Zr has a peak with $M_\gamma \approx 2$ at $E \approx 1.5$ MeV. This is mainly due to the first 4^+ state that decay via the 2^+ state into the ground state, giving $M_\gamma = 2$. At about the same excitation energy, Fig. 1(b) shows the decay path of the first 0^+ state, which also goes via the 2^+ state, giving multiplicity $M_\gamma = 2$.

The energy distribution of first-generation or primary γ rays can be extracted from the unfolded total γ-ray spectra of Figs. 1(a) and 1(b). Let $U^E(E_\gamma)$ be the unfolded γ-ray spectrum at a certain initial excitation energy E. Then the primary spectrum can be obtained by a subtraction of a weighted sum of $U^{E'}(E_\gamma)$ spectra for E' below E:

$$F^E(E_\gamma) = U^E(E_\gamma) - \sum_{E' < E} w_{E'} U^{E'}(E_\gamma). \qquad (3)$$

The weighting coefficients $w_{E'}$ are determined by iterations as described in Ref. [16]. After a few iterations, the multiplicity of the primary spectrum should be $M(F^E) \approx 1$, where the multiplicity of the total spectrum is determined by $M(U^E) = M_\gamma^E(E)$ from Eq. (1). The obtained primary spectra are organized into a matrix $P(E_\gamma, E)$ that is normalized according to $\sum_{E_\gamma} P(E_\gamma, E) = 1$.
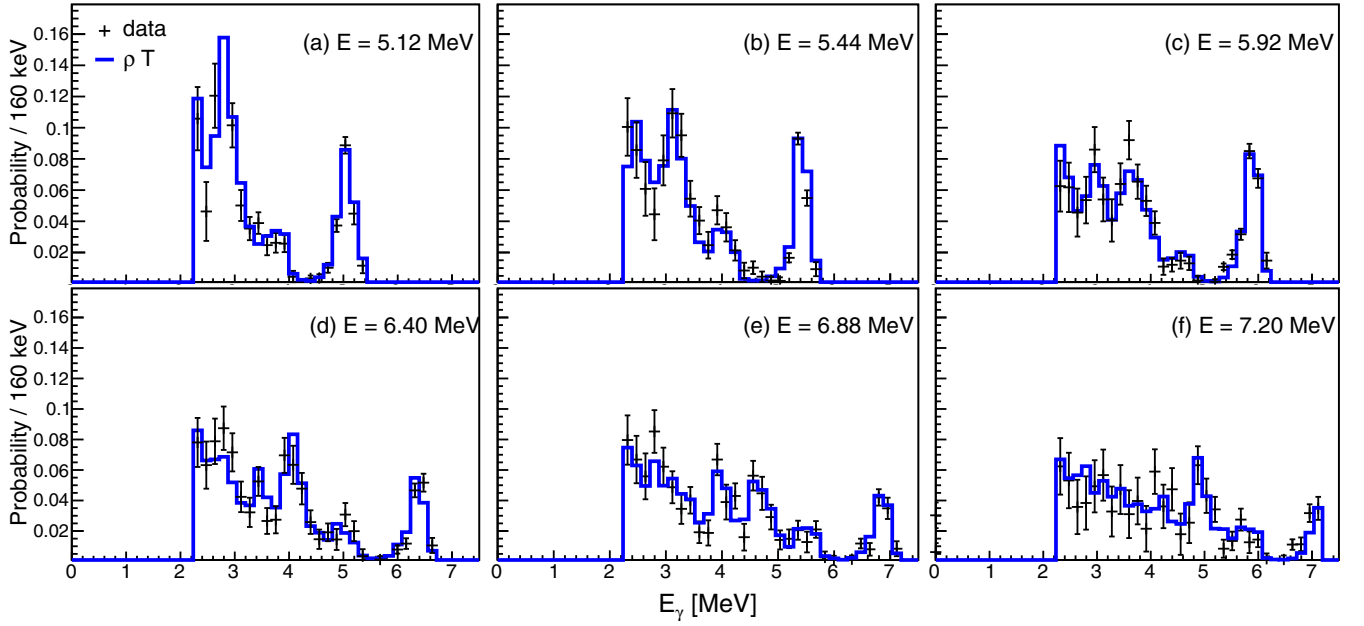
FIG. 4. Primary γ-ray spectra from various initial excitation energies E (crosses) in ^{91}Zr. The spectra are compared to the product $\rho(E - E_\gamma)\mathscr{T}(E_\gamma)$ (blue histogram). Both the γ and excitation energy dispersions are 160 keV/ch.

The next step of the Oslo method is the factorization

$$P(E_\gamma, E) \propto \rho(E - E_\gamma)\mathscr{T}(E_\gamma), \qquad (4)$$

where we assume that the decay probability is proportional to the NLD at the final energy $\rho(E - E_\gamma)$ according to Fermi's golden rule [19,20]. The decay is also proportional to the γ-ray transmission coefficient $\mathscr{T}$, which is assumed to be independent of excitation energy according to the Brink hypothesis [21,22].

The relation (4) makes it possible to simultaneously extract the two one-dimensional vectors ρ and $\mathscr{T}$ from the two-

dimensional landscape P. We use the iteration procedure of Schiller *et al.* [23] to determine ρ and $\mathscr{T}$ by a least χ^2 fit using relation (4). For this extraction, we have chosen the following part of the P matrix: For ^{91}Zr the excitation energy region is 5.0 MeV $< E <$ 7.2 MeV with $E_\gamma >$ 2.4 MeV, and for ^{92}Zr we choose 4.5 MeV $< E <$ 8.6 MeV with $E_\gamma >$ 1.5 MeV.

The applicability of relation (4) and the quality of the fitting procedure are demonstrated in Figs. 4 and 5 for ^{91,92}Zr, respectively. The agreement is satisfactory when one keeps in mind that the γ-decay pattern fluctuates from level to level. With the rather narrow excitation energy bins of 160
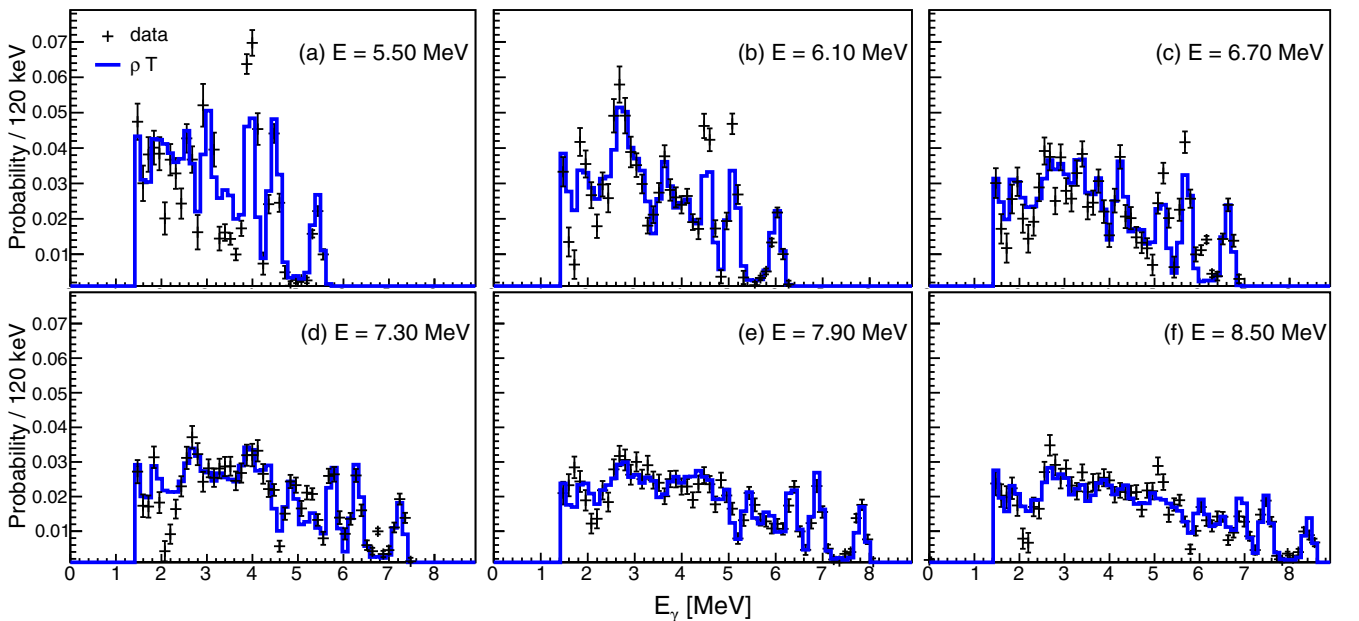

FIG. 5. Same as Fig. 4 for ^{92}Zr. Both the γ and excitation energy dispersions are 120 keV/ch.

TABLE I. Experimental level spacings and average γ widths for $\ell = 0$ neutron capture experiments [26,27]. For the evaluation of $\langle\Gamma_{\gamma0}\rangle$ of ^{91}Zr, additional resonances from Ref. [28] were added; see text.

Nucleus Ref.	S_n [MeV]	D_0 [eV] [26,27]	$\langle\Gamma_{\gamma0}\rangle$ [meV] [28]	$\langle\Gamma_{\gamma0}\rangle$ [meV] [29]	$\langle\Gamma_{\gamma0}\rangle_B$ [meV] [26–28]	$\langle\Gamma_{\gamma0}\rangle_B$ [meV] Adopted
^{91}Zr	7.195	7179(233)	170(20)	130(20)	180(137)	130(40)
^{92}Zr	8.635	514(15)	140(40)	134(16)	131(56)	140(40)

and 120 keV for ^{91,92}Zr, respectively, each γ-ray spectrum will be subject to significant Porter-Thomas fluctuations [24] responsible for local deviations for individual primary spectra compared to the global average given by $\rho\mathscr{T}$. It should be mentioned that only the spectra from a few excitation energy bins are shown; however, all spectra show the same agreement with $\rho\mathscr{T}$. Further tests and justification of the Oslo method have been discussed in Ref. [25].

III. THE NUCLEAR LEVEL DENSITY

The functional form of ρ and $\mathscr{T}$ are uniquely identified through the fit, but the scale and slope of these functions are still undetermined. It is shown in Ref. [23] that functions generated by the transformations

$$\tilde{\rho}(E - E_\gamma) = A \exp[\alpha(E - E_\gamma)] \, \rho(E - E_\gamma), \quad (5)$$

$$\tilde{\mathscr{T}}(E_\gamma) = B \exp(\alpha E_\gamma)\mathscr{T}(E_\gamma) \quad (6)$$

give identical fits to the primary γ-ray spectra, as shown by the examples in Figs. 4 and 5. In the following, we will estimate the parameters A and α from systematics and other experimental data. The normalization of $\mathscr{T}$ by the constant B only concerns the γ SF that will be discussed in the next subsection.

The normalization of the NLD is determined by known levels at low excitation energies and the NLD at the neutron separation energy $\rho(S_n)$, which can be estimated from the s-wave resonance spacing D_0 [26,27], as listed in Table I. However, such an extraction requires knowledge of the spin and parity distributions of the NLD at the neutron separation energy and is consequently model dependent. For these reasons, two different NLD formulations are considered, namely the constant-temperature (CT) formula [29,30] and the Hartree-Fock-Bogolyubov (HFB) plus combinatorial model [31], which give two quite different descriptions of the energy, spin, and parity dependences of the NLD. In the case of the HFB plus combinatorial model, the NLD is tabulated and its spin and parity distributions are determined by the underlying effective interaction. The total NLD $\rho(S_n)$ deduced from the s-wave resonance spacings are given in Table II. Note that the HFB plus combinatorial model predicts that the NLD equiparity is achieved only above the neutron separation energy, at typically 9 MeV, in both ^{91,92}Zr.

In contrast, the CT formula is bound to assume an equiparity distribution and to follow a spin distribution given by [32]

$$g(E, I) \simeq \frac{2I + 1}{2\sigma^2(E)} \exp[-(I + 1/2)^2/2\sigma^2(E)], \quad (7)$$

where $E = S_n$ at the neutron binding energy, I is the spin, and $\sigma(E)$ is the energy-dependent spin cutoff parameter, which

turns out to be the main contributor to the uncertainties in the estimate of the total NLD. The spin cutoff parameter σ is traditionally determined by a close-to-rigid moment of inertia. Since $\sigma^2 = \Theta T/\hbar^2$ [32] and the nuclear temperature T is assumed to be approximately constant for $2\Delta < E < S_n$ [33,34], σ^2 follows the energy dependence of the moment of inertia Θ. We assume that Θ is proportional to the number of quasiparticles, which again is proportional to E. Thus, we write

$$\sigma^2(E) = \sigma_d^2 + \frac{E - E_d}{S_n - E_d}\big[\sigma^2(S_n) - \sigma_d^2\big], \quad (8)$$

which goes through two anchor points. The first point σ_d^2 is determined from known discrete levels at excitation energy $E = E_d$. The second point at $E = S_n$ is estimated assuming a rigid moment of inertia [35]:

$$\sigma^2(S_n) = 0.0146 A^{5/3}\frac{1 + \sqrt{1 + 4aU_n}}{2a}, \quad (9)$$

where A is the mass number, and $U_n = S_n - E_1$ is the intrinsic excitation energy. The level NLD parameter a and the energy shift parameter E_1 is determined according to Ref. [35].

In order to obtain a systematic error band, we multiply the rigid moment of inertia $\Theta_{\text{rigid}} = 0.0146 A^{5/3}$ of Eq. (9) with a factor η, which takes the values $\eta = 0.6, 0.8$, and 1.0 for the low (L), recommended (R), and high (H) values, respectively. The corresponding spin cutoff parameters and NLDs are listed in Table III.

Comparing Tables II and III, the HFB plus combinatorial model predicts significantly higher total NLD at S_n that can hardly be taken into account by the parameter uncertainties in the CT approach. Both approaches will consequently be considered in the present analysis, not only for determining the NLD, but also the corresponding γ-ray strength function, as detailed below.

When $\rho(S_n)$ is estimated, we still need to bridge the energy gap between our data points and the estimated $\rho(S_n)$ value. To do so, we use the corresponding NLD formula, i.e., the HFB

TABLE II. Total ^{91,92}Zr NLDs at the neutron separation energy deduced with the HFB plus combinatorial model from the experimental s-wave spacing D_0 and its uncertainties, indicated by low (L), recommended (R), and high (H).

Nucleus	$\rho_L(S_n)$ [MeV^{-1}]	$\rho_R(S_n)$ [MeV^{-1}]	$\rho_H(S_n)$ [MeV^{-1}]
^{91}Zr	7200	7440	7700
^{92}Zr	19 560	20 120	20 700

TABLE III. Parameters used to extract NLDs within the CT model approach. Systematic uncertainties are indicated by low (L), recommended (R), and high (H) values (see text).

Nucleus	a [MeV^{-1}]	E_1 [MeV]	E_d [MeV]	σ_d	$\sigma_L(S_n)$	$\sigma_R(S_n)$	$\sigma_H(S_n)$	$\rho_L(S_n)$ [MeV^{-1}]	$\rho_R(S_n)$ [MeV^{-1}]	$\rho_H(S_n)$ [MeV^{-1}]	T_{CT} [MeV]	E_0 [MeV]
^{91}Zr	9.84	−0.03	2.5	3.1(2)	3.83	4.42	4.95	4230(140)	5590(180)	6950(230)	0.88(5)	−0.29(48)
^{92}Zr	10.44	0.66	3.0	3.0(2)	3.89	4.50	5.03	13500(390)	16640(490)	19840(580)	0.90(2)	−0.02(21)

plus combinatorial model in the first case and the CT formula in the second case [32],

$$\rho(E) = \frac{1}{T_{CT}} \exp\left(\frac{E - E_0}{T_{CT}}\right), \qquad (10)$$

where the temperature T_{CT} and energy shift E_0 are free parameters adjusted to the data and given in Table III for the two Zr isotopes.

The experimental NLDs for ^{91,92}Zr are shown in Fig. 6 for the CT approach and the HFB plus combinatorial model. In both cases, a rather CT pattern is found for the total NLD above typically 3 MeV, though their respective slopes are different following different predictions of the total NLD at S_n.
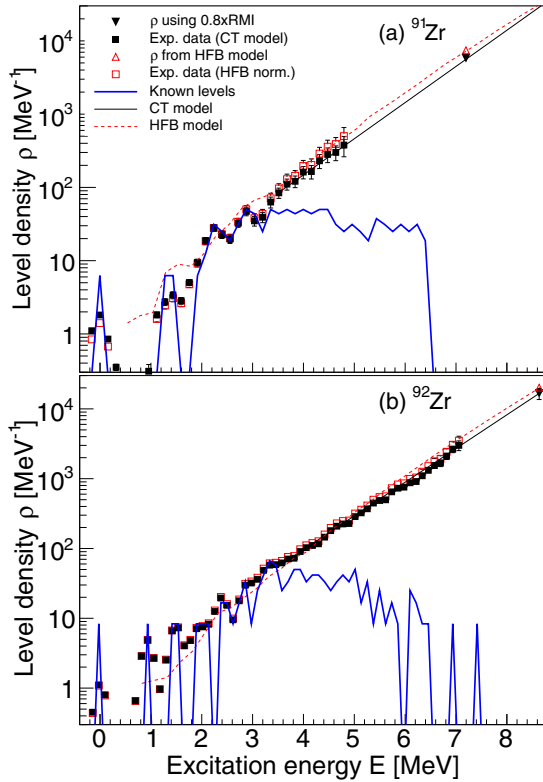

FIG. 6. Normalized NLDs of ^{91,92}Zr extracted from the present experiment. At low excitation energies, the data are normalized to known discrete levels (solid blue line). At higher excitation energies, the data are normalized to ρ at S_n using resonance spacing D_0. Two normalization procedures for $\rho(S_n)$ are used: (i) the spin cutoff parameter listed in Table III together with the CT NLD parameters (black lines and symbols) and (ii) the HFB plus combinatorial model (red dashed lines and symbols) [31].

IV. THE γ-RAY STRENGTH FUNCTION

The standard way to determine the remaining normalization coefficient B of Eq. (6) is to constrain the data to the known total radiative width $\langle\Gamma_{\gamma 0}\rangle$ at S_n [23,36], defined as

$$\langle\Gamma_{\gamma 0}(S_n)\rangle = \frac{1}{2\pi\rho(S_n, I, \pi)} \sum_{I_f} \int_0^{S_n} dE_\gamma \mathscr{T}(E_\gamma)$$
$$\times \rho(S_n - E_\gamma, I_f), \qquad (11)$$

where the summation and integration run over all final levels with spin I_f that are accessible by $E1$ or $M1$ transitions with energy E_γ. This procedure is known to work well when the individual γ widths are centered around a common average value.

Columns 4 and 5 in Table I list the experimental $\langle\Gamma_{\gamma 0}\rangle$ values from literature [28,29]. However, Fig. 7 shows that the individual γ widths scatter much more than the experimental uncertainties for the individual γ widths, which are usually below ≈ 20 meV. For ^{91}Zr, we can hardly locate a common average $\langle\Gamma_{\gamma 0}\rangle$ as the data scatter from 5.5 to 590 meV. Thus, the standard method of calculating weighted average and uncertainties give unrealistic small errors in the case of ^{91}Zr.
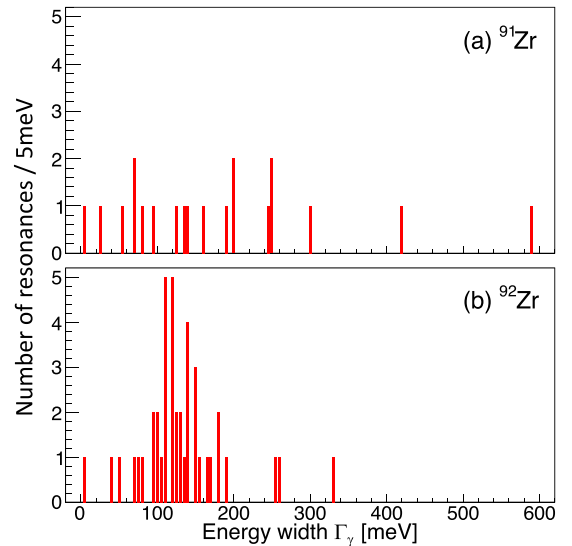

FIG. 7. The number of $\ell = 0$ resonances as function of their specific γ width Γ_γ. For ^{91}Zr, 15 resonances are taken from Ref. [26] and an additional 5 from Ref. [28]. For ^{92}Zr, the 42 resonances are taken from Ref. [27]. The data are used to re-evaluate the average γ width, called $\langle\Gamma_{\gamma 0}\rangle_B$ in column 6 of Table I.

Therefore, we calculate instead the mean average of the γ widths and the standard deviation of these values by

$$\langle \Gamma_{\gamma 0} \rangle_B = \frac{1}{n} \sum_{i=1}^{n} \Gamma_{\gamma 0}^i, \qquad (12)$$

$$\Delta \langle \Gamma_{\gamma 0} \rangle_B = \sqrt{\frac{1}{n-1} \sum_{i=1}^{n} \left(\Gamma_{\gamma 0}^i - \langle \Gamma_{\gamma 0} \rangle_B \right)^2}, \qquad (13)$$

where n is the number of resonances. The index B indicates that these values are relevant for the determination of the coefficient B. For ^{92}Zr, we find reasonably consistent values of the average γ widths in columns 4, 5, and 6 of Table I and adopt the value $\langle \Gamma_{\gamma 0} \rangle_B = 140 \pm 40$ meV. As expected, the uncertainty in the average γ width for ^{91}Zr is very large.

To constrain the ^{91}Zr data further, we use the photonuclear reaction data [7,37] around S_n to determine the B value. The transformation from photonuclear cross section σ_γ to γSF is performed by [29]

$$f(E_\gamma) = \frac{1}{3\pi^2 \hbar^2 c^2} \frac{\sigma_\gamma(E_\gamma)}{E_\gamma}. \qquad (14)$$

Note that the photoneutron cross section in the direct vicinity of the neutron threshold is not considered to estimate the corresponding γSF, since in this region it remains also sensitive to the neutron channel and the γSF can consequently not be deduced from the cross section in an unambiguous way.

In turn, the dipole γSF, including both the $E1$ and $M1$ contributions, can be calculated from our measured transmission coefficient [29] through

$$f(E_\gamma) = \frac{1}{2\pi} \frac{\mathcal{T}(E_\gamma)}{E_\gamma^3}. \qquad (15)$$

The corresponding experimental γSFs for ^{91,92}Zr are displayed as solid squares in Fig. 8. The figure also includes the γSFs derived from ^{91,92}Zr(γ, n) cross section data by Utsunomiya *et al.* [7] and Berman *et al.* [37]. As mentioned above, we have normalized our ^{91}Zr data points to match the (γ,n) data at S_n, as shown in Fig. 8. The adopted $\langle \Gamma_{\gamma 0} \rangle_B$ values used to normalize the γSF and estimate the uncertainies are given in column 7 of Table I.

Since our dipole strength includes both the $E1$ and $M1$ contributions, for estimating the average radiative width $\langle \Gamma_{\gamma 0} \rangle$ as well as the radiative neutron capture cross section of ^{90}Zr, they need to be disentangled, especially in view of the nonequiparity of the NLD predicted within the HFB plus combinatorial approach [31]. For this purpose, we have estimated the spin-flip $M1$ resonance from two different approaches, namely the HFB plus quasiparticle random-phase approximation (QRPA) based on the Gogny D1M interaction [38] and a Lorentzian function, both guided by a previous experimental analysis of photoneutron measurements [7] as well as (p, p') scattering data on ^{90}Zr close to $\theta = 0$ deg [8]. Such experiments revealed an $M1$ resonance located at a centroid energy $E_{M1} \simeq 9$–9.5 MeV with a width $\Gamma_{M1} \simeq 2.50$ MeV. At almost the same energies, an $E1$ pygmy resonance with $E_{PDR1} = 9.2$ MeV and $\Gamma_{PDR1} = 2.9$ MeV has been found. Such structures at around 9.5 MeV have been reported also
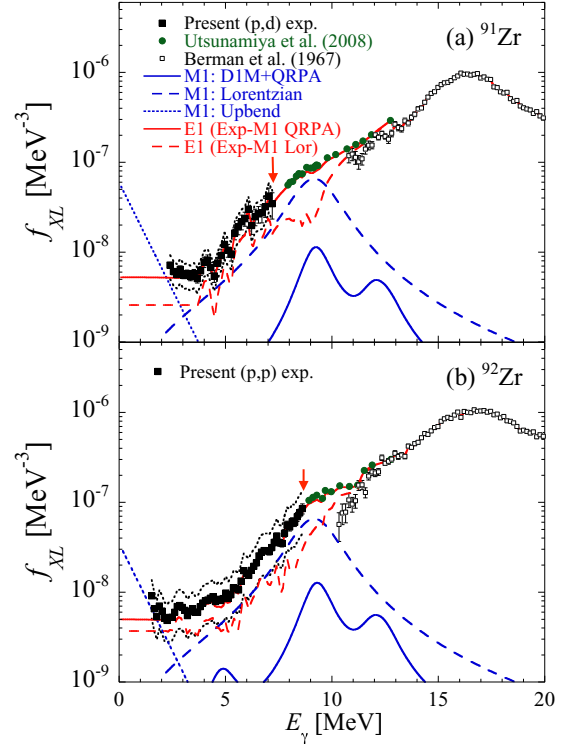

FIG. 8. (a) Experimental ^{91}Zr γSFs (solid squares) with its error band (dotted lines) due to the uncertainty in σ, D_0, and $\langle \Gamma_{\gamma 0} \rangle$ (see Table III). Also shown are the photoneutron data [7,37], the spin-flip $M1$ strength derived from either D1M+QRPA calculations (solid blue line) or a Lorentzian function (dashed blue line), and the $M1$ upbend (dotted blue line). The resulting recommended $E1$ strength is shown by a solid (dashed) red line and obtained from the total experimental dipole strength by subtracting the D1M+QRPA (Lorentzian) $M1$ component. The neutron separation energies are indicated by arrows. (b) Same for the ^{92}Zr γSFs.

for the ^{92,94,96}Zr isotopes [39]. For our sensitivity analysis, we consider both options, i.e., possible $M1$ representations, including a strong $M1$ Lorentzian with a peak cross section $\sigma_0 = 7$ mb [7], as well as the D1M+QRPA strength, as shown in Fig. 8. The D1M+QRPA strength is seen to be significantly less than the phenomenological Lorentzian strength inferred in Ref. [7], giving rise to a stronger possible $E1$ counterpart.

Finally, our measurements at the lowest energies (i.e., around 2 MeV) also suggest the presence of a low-energy enhancement (the so-called upbend) that has been suggested by shell-model calculations to be of $M1$ nature [40,41]. For nuclei studied in this mass region with the Oslo method, we find a low-energy enhancement (upbend) of the γSF [42–46]. The upbend has also been verified for ^{96}Mo using another technique [47].

To describe the low-energy enhancement, it is therefore important to include below 2 MeV an $M1$ upbend that may influence not only the estimate of the total radiative width $\langle \Gamma_{\gamma 0} \rangle$, but also the radiative neutron capture cross section. The upbend structure is described by the exponential function
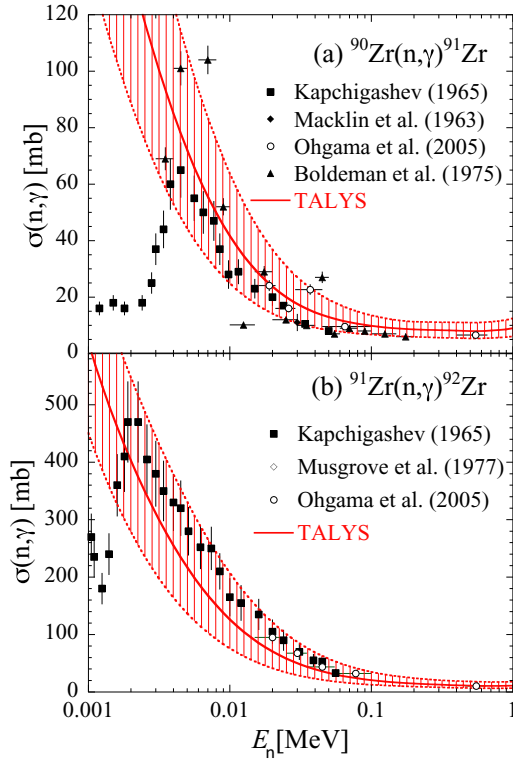
FIG. 9. (a) Comparison between the experimental ^{90}Zr$(n,\gamma)^{91}$Zr cross section [50–52] and the one obtained with the TALYS code on the basis of the NLD and γSF derived experimentally in the present work. The hashed area depicts all the experimental and model-dependent uncertainties taken into account in the present analysis. (b) Same for ^{91}Zr$(n,\gamma)^{92}$Zr cross section with experimental data taken from Refs. [50,52,53].

[41,44]

$$f_{\text{upbend}}(E_\gamma) = C \exp(-\eta E_\gamma). \qquad (16)$$

The adopted parameters $C = 5 \pm 2 \times 10^{-8}$ MeV^{-3} and $\eta = 1.1 \pm 0.5$ MeV are used for modeling the upbend of ^{91}Zr and $C = 3.5 \pm 0.5 \times 10^{-8}$ MeV^{-3} and $\eta = 1.1 \pm 0.5$ MeV are used for ^{92}Zr.

With this procedure, it is possible to disentangle from experimental data the $E1$ and $M1$ components together with their relative model uncertainties for a sensitivity analysis. The resulting $E1$ strengths deduced from the experimental strength by subtracting the D1M+QRPA or Lorentzian spin-flip $M1$ contribution as well as the low-energy $M1$ upbend are shown in Fig. 8 for both Zr isotopes. Note that a constant $E1$ strength function is assumed for energies $E_\gamma \rightarrow 0$, as indicated by shell-model calculations [48] and empirically described by the generalized Lorentzian approach [49].

With these resulting $E1$ and $M1$ strengths and NLD (as detailed in Sec. III), we obtain for ^{91}Zr a $\langle \Gamma_{\gamma 0} \rangle_B = 130 \pm 40$ meV, after normalizing our ^{91}Zr data points to match the (γ,n) data at S_n. As mentioned above for ^{92}Zr, we adopt $\langle \Gamma_{\gamma 0} \rangle_B = 140 \pm 40$ MeV to constrain the experimental dipole strength.
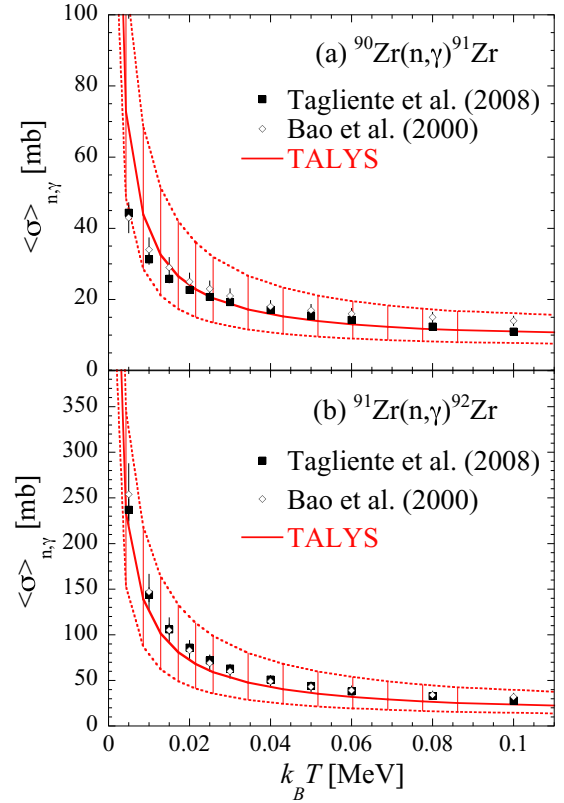

FIG. 10. Comparison between the experimental ^{90}Zr$(n,\gamma)^{91}$Zr Maxwellian-averaged cross section [26,54] and the one obtained with the TALYS code on the basis of the NLD and γSF derived experimentally in the present work. (b) Same for ^{91}Zr$(n,\gamma)^{92}$Zr Maxwellian-averaged cross section with experimental data taken from Refs. [27,54].

V. THE RADIATIVE NEUTRON CAPTURE CROSS SECTIONS

The NLD and γSF derived in the previous sections can now be tested on the additional experimental data relative to the radiative neutron-capture cross sections ^{90}Zr$(n,\gamma)^{91}$Zr and ^{91}Zr$(n,\gamma)^{92}$Zr. These cross sections essentially depend on the photon transmission coefficient of the final compound nucleus, hence to the NLD and γSF obtained from the present experiments. We compare in Fig. 9 the experimentally known (n,γ) cross sections with the theoretical calculations obtained with the TALYS reaction code [12]. Both cross-section calculations use directly the $E1$ and $M1$ strength functions derived in Sec. IV, assuming that the $M1$ spin-flip resonance is given either by the D1M+QRPA or the Lorentzian strength and including an additional $M1$ upbend. In all cases, the γSF is firmly constrained by our dipole strength, with its lower and upper values determined on the basis of the uncertainties affecting not only the $M1 - E1$ decomposition, but also the average radiative width $\langle \Gamma_{\gamma 0} \rangle$ and s-wave resonance spacing D_0. Similarly, the NLD as derived in Sec. III are modeled either by the HFB plus combinatorial model or the CT formula, and in each case constrained on the experimental D_0 value with its upper and lower values. It should be mentioned that

the upper (lower) limit for the NLD [i.e., lower (upper) value of the experimental D_0] is directly correlated to the upper (lower) limit for the derived dipole γSF, as constrained by the $\langle\Gamma_{\gamma0}\rangle$. The careful account of all these uncertainties is translated into the hashed area displayed in Fig. 9.

A similar comparison is made for the Maxwellian-averaged cross sections in Fig. 10. The upper cross sections are found with the upper value of the γSF obtained with the D1M+QRPA model of the $M1$ strength, while the lower cross section corresponds to the lower value based on the $M1$ Lorentzian representation.

The main uncertainties in the present analysis stem from the $E1$–$M1$ decomposition as well as the normalization of the experimental γSF. Note that the intrinsic model uncertainties, using all available NLD and γSF models in TALYS, yield a factor $\sim$10 between the minimum and maximum (n,γ) cross sections in this mass region [43]. Thus, although our indirect method gives a rather large error band, it is still a significant improvement compared to the range of possible values from the unconstrained model predictions. This analysis shows that the NLD and γSF derived in the present work are fully compatible with the experimental radiative neutron-capture cross sections and can therefore be expected to be a good representation of the statistical properties of the de-exciting compound nuclei ^{91}Zr and ^{92}Zr.

VI. SUMMARY AND OUTLOOK

NLDs and γSFs of ^{91,92}Zr have been extracted from particle-γ coincidence data using the Oslo method. The data are normalized to neutron-resonance data and (γ,n) cross section data, taking into account systematic errors due to uncertain nuclear spin distributions as well as uncertainties in the extraction procedure and the external normalization data. Moreover, the γSFs are decomposed into their $E1$ and $M1$ components based on state-of-the-art microscopic calculations of the $M1$ strength, as well as a phenomenological description of the $M1$ spin-flip resonance guided by previous (p,p') measurements.

Our data, including all the possible normalization uncertainties, have been used as input for calculating ^{90,91}Zr(n,γ) cross sections and MACS of relevance for the $A\sim90$ s-process peak. We found that our indirect method of determining the MACS is fully compatible with direct measurements, giving confidence that this approach is capable of providing reasonable cross sections for cases where direct measurements are not available, such as the branch-point nucleus ^{95}Zr. In the future, we will perform experiments at OCL to measure the ^{96}Zr NLD and γSF to deduce a first experimentally constrained ^{95}Zr(n,γ) cross section and MACS.

[1] E. M. Burbidge, G. R. Burbidge, W. A. Fowler, and F. Hoyle, Rev. Mod. Phys. **29**, 547 (1957).

[2] A. G. W. Cameron, Publ. Astron. Soc. Pac. **69**, 201 (1957).

[3] M. Arnould, S. Goriely, and K. Takahashi, Phys. Rep. **450**, 97 (2007).

[4] F. Käppeler, R. Gallino, S. Bisterzo, and W. Aoki, Rev. Mod. Phys. **83**, 157 (2011), and references therein.

[5] W. Hauser and H. Feshbach, Phys. Rev. **87**, 366 (1952).

[6] M. Lugaro, F. Herwig, J. C. Lattanzio, R. Gallino, and O. Straniero, Astrophys. J. **586**, 1305 (2003).

[7] H. Utsunomiya, S. Goriely, T. Kondo, T. Kaihori, A. Makinaga, S. Goko, H. Akimune, T. Yamagata, H. Toyokawa, T. Matsumoto *et al.*, Phys. Rev. Lett. **100**, 162502 (2008).

[8] C. Iwamoto, H. Utsunomiya, A. Tamii, H. Akimune, H. Nakada, T. Shima, T. Yamagata, T. Kawabata, Y. Fujita, H. Matsubara *et al.*, Phys. Rev. Lett. **108**, 262501 (2012).

[9] P. Neyskens, S. Van Eck, A. Jorissen, S. Goriely, L. Siess, and B. Plez, Nature (London) **517**, 174 (2015).

[10] G. Tagliente, P. M. Milazzo, K. Fujii, U. Abbondanno, G. Aerts, G. H. Álvarez, F. Alvarez-Velarde, S. Andriamonje, J. Andrzejewski, and L. Audouin *et al.*, Phys. Rev. C **87**, 014622 (2013).

[11] M. Lugaro, G. Tagliente, A. I. Karakas, P. M. Milazzo, F. Käppeler, A. M. Davis, and M. R. Savina, Astrophys. J. **780**, 95 (2014).

[12] A. J. Koning and D. Rochman, Nucl. Data Sheets **113**, 2841 (2012).

[13] M. Guttormsen, A. Bürger, T. E. Hansen, and N. Lietaer, Nucl. Instrum. Methods Phys. Res. A **648**, 168 (2011).

[14] M. Guttormsen, A. Atac, G. Løvhøiden, S. Messelt, T. Ramsøy, J. Rekstad, T. F. Thorsteinsen, T. S. Tveter, and Z. Zelazny, Phys. Scr. **T32**, 54 (1990).

[15] M. Guttormsen, T. S. Tveter, L. Bergholt, F. Ingebretsen, and J. Rekstad, Nucl. Instrum. Methods Phys. Res. A **374**, 371 (1996).

[16] M. Guttormsen, T. Ramsøy, and J. Rekstad, Nucl. Instrum. Methods Phys. Res. A **255**, 518 (1987).

[17] Data from the NNDC On-Line Data Service database, http://www.nndc.bnl.gov/nudat2/

[18] H. P. Blok, L. Hulstman, E. J. Kaptein, and J. Blok, Nucl. Phys. A **273**, 142 (1976).

[19] P. A. M. Dirac, Proc. Royal Soc. London, Ser. A **114**, 243 (1927).

[20] E. Fermi, *Nuclear Physics* (University of Chicago Press, Chicago, 1950).

[21] D. M. Brink, doctoral thesis, Oxford University, Oxford, UK, 1955 (unpublished).

[22] M. Guttormsen, A. C. Larsen, A. Görgen, T. Renstrøm, S. Siem, T. G. Tornyi, and G. M. Tveten, Phys. Rev. Lett. **116**, 012502 (2016).

[23] A. Schiller, L. Bergholt, M. Guttormsen, E. Melby, J. Rekstad, and S. Siem, Nucl. Instrum. Methods Phys. Res. A **447**, 498 (2000).

[24] T. Porter and R. G. Thomas, Phys. Rev. **104**, 483 (1956).

[25] A. C. Larsen, M. Guttormsen, M. Krtička, E. Běták, A. Bürger, A. Görgen, H. T. Nyhus, J. Rekstad, A. Schiller, S. Siem *et al.*, Phys. Rev. C **83**, 034315 (2011).

[26] G. Tagliente, K. Fujii, P. M. Milazzo, C. Moreau, G. Aerts, U. Abbondanno, H. Álvarez, F. Alvarez-Velarde, S. Andriamonje, J. Andrzejewski *et al.*, Phys. Rev. C **77**, 035802 (2008).

[27] G. Tagliente, P. M. Milazzo, K. Fujii, G. Aerts, U. Abbondanno, H. Álvarez, F. Alvarez-Velarde, S. Andriamonje, J. Andrzejewski, P. Assimakopoulos *et al.*, Phys. Rev. C **78**, 045804 (2008).

[28] S. F. Mughabghab, *Atlas of Neutron Resonances*, 5th ed. (Elsevier Science, Amsterdam, 2006).

[29] R. Capote, M. Herman, P. Oblozinsky *et al.*, Nucl. Data Sheets **110**, 3107 (2009); Reference Input Library RIPL-3, http://www-nds.iaea.org/RIPL-3/

[30] A. J. Koning, S. Hilaire, and S. Goriely, Nucl. Phys. A **810**, 13 (2008).

[31] S. Goriely, S. Hilaire, and A. J. Koning, Phys. Rev. C **78**, 064307 (2008).

[32] T. Ericson, Nucl. Phys. A **11**, 481 (1959).

[33] L. G. Moretto, A. C. Larsen, F. Giacoppo, M. Guttormsen, S. Siem, and A. V. Voinov, J. Phys.: Conf. Ser. **580**, 012048 (2015).

[34] M. Guttormsen *et al.*, Eur. Phys. J. A **51**, 170 (2015).

[35] T. von Egidy and D. Bucurescu, Phys. Rev. C **72**, 044311 (2005); **73**, 049901(E) (2006).

[36] A. Voinov, M. Guttormsen, E. Melby, J. Rekstad, A. Schiller, and S. Siem, Phys. Rev. C **63**, 044313 (2001).

[37] B. L. Berman *et al.*, Phys. Rev. **162**, 1098 (1967).

[38] V. Tselyaev, N. Lyutorovich, J. Speth, S. Krewald, and P.-G. Reinhard, Phys. Rev. C **94**, 034306 (2016).

[39] A. Tamii, COMEX5 2015, http://comex5.ifj.edu.pl/slides/tamii.pdf

[40] B. A. Brown and A. C. Larsen, Phys. Rev. Lett. **113**, 252502 (2014).

[41] R. Schwengner, S. Frauendorf, and A. C. Larsen, Phys. Rev. Lett. **111**, 232504 (2013).

[42] M. Guttormsen, R. Chankova, U. Agvaanluvsan, E. Algin, L. A. Bernstein, F. Ingebretsen, T. Lönnroth, S. Messelt, G. E. Mitchell, J. Rekstad *et al.*, Phys. Rev. C **71**, 044307 (2005).

[43] A. C. Larsen, M. Guttormsen, R. Schwengner, D. L. Bleuel, S. Goriely, S. Harissopulos, F. L. Bello Garrote, Y. Byun, T. K. Eriksen, F. Giacoppo *et al.*, Phys. Rev. C **93**, 045810 (2016).

[44] A. Spyrou, S. N. Liddick, A. C. Larsen, M. Guttormsen, K. Cooper, A. C. Dombos, D. J. Morrissey, F. Naqvi, G. Perdikakis, S. J. Quinn *et al.*, Phys. Rev. Lett. **113**, 232502 (2014).

[45] T. Renstrøm, H.-T. Nyhus, H. Utsunomiya, R. Schwengner, S. Goriely, A. C. Larsen, D. M. Filipescu, I. Gheorghe, L. A. Bernstein, D. L. Bleuel *et al.*, Phys. Rev. C **93**, 064302 (2016).

[46] G. M. Tveten, A. Spyrou, R. Schwengner, F. Naqvi, A. C. Larsen, T. K. Eriksen, F. L. Bello Garrote, L. A. Bernstein, D. L. Bleuel, L. Crespo Campo *et al.*, Phys. Rev. C **94**, 025804 (2016).

[47] M. Wiedeking, L. A. Bernstein, M. Krticka, D. L. Bleuel, J. M. Allmond, M. S. Basunia, J. T. Burke, P. Fallon, R. B. Firestone, B. L. Goldblum *et al.*, Phys. Rev. Lett. **108**, 162503 (2012).

[48] K. Sieja (private communication).

[49] J. Kopecky and M. Uhl, Phys. Rev. C **41**, 1941 (1990).

[50] S. P. Kapchigashev, Atomnaya Energiya **19**, 294 (1965)

[51] R. L. Macklin, T. Inada, and J. H. Gibbons, Bull. Am. Phys. Soc. **8**, 81 (1963).

[52] K. Ohgama, M. Igashira, and T. Ohsaki, J. Nucl. Sci. Technol. **42**, 333 (2005).

[53] A. R. DeL. Musgrove, J. W. Boldeman, B. J. Allen, J. A. Harvey, and R. L. Macklin, Aust. J. Phys. **30**, 391 (1977).

[54] Z. Y. Bao, H. Beer, F. Käppeler, F. Voss, K. Wisshak, and T. Rauscher, At. Data Nucl. Data Tables **76**, 70 (2000).